

## Research Article

# Experimental evidence of disorder enhanced electron-phonon scattering in graphene devices



Charalambos Evangelis<sup>a,\*</sup>, Edward McCann<sup>b,1</sup>, Jacob L. Swett<sup>a</sup>, Sumit Tewari<sup>a</sup>, Xinya Bian<sup>a</sup>, James O. Thomas<sup>a</sup>, G. Andrew D. Briggs<sup>a</sup>, Oleg V. Kolosov<sup>b,\*\*</sup>, Jan A. Mol<sup>c</sup>

<sup>a</sup> Department of Materials, University of Oxford, Parks Road, OX1 3PH, Oxford, UK

<sup>b</sup> Department of Physics, Lancaster University, Bailrigg, LA1 4YB, Lancaster, UK

<sup>c</sup> School of Physics and Astronomy, Queen Mary University of London, London, E1 4NS, UK

## ARTICLE INFO

## Article history:

Received 3 September 2020

Received in revised form

13 November 2020

Accepted 4 December 2020

Available online 9 December 2020

## Keywords:

Graphene

Disorder

Scattering rate

Room temperature

High current density

Phonon

## ABSTRACT

Induced disorder in graphene enables changes in electrical and thermal transport. It has been shown previously that disorder is very important for electron cooling in graphene through disorder-assisted electron-phonon scattering, particularly via the supercollisions process. Here we study electron-momentum relaxation due to electron-phonon scattering while increasing the degree of disorder. With in-situ scanning thermal microscopy we monitor the temperature rise in the constriction region of a bowtie-shaped graphene device while increasing the disorder by means of feedback-controlled voltage ramps at high-current densities. Analysis of the combined thermal and electrical measurements in the low bias regime shows that the relative change of the momentum scattering rate vs temperature, as measured at room temperature, increases with strong local disorder. By excluding other candidate mechanisms for this phenomenon, including a change of the charge carriers density and activation of optical phonons, we conclude that the increase we observe in the temperature-dependent component of the scattering rate is likely due to new acoustic phonon scattering channels that open up as disorder increases.

© 2020 Elsevier Ltd. All rights reserved.

## 1. Introduction

Understanding momentum relaxation mechanisms of electrons with different degrees of disorder, especially at room temperature, is of prime importance for many electronic applications of graphene and other van-der-Waals conductive materials. For example, the use of graphene as an interconnect in next generation electronics, including CMOS [1], necessitates high electrical currents while requiring efficient heat dissipation to avoid breakdown [2]. Under high-current density, graphene is Joule-heated to extremely high temperatures. Electron mobility is limited due to electron scattering by phonons and disorder (including impurities, defects, and vacancies) [3], and, as a result, the current saturates and the temperature rises. High temperature results in oxidation of

graphene in air, or sublimation in vacuum, which ultimately leads to the breakdown of the material [4,5]. In some cases, high temperature can also be catastrophic for the underlying substrate, due to a lower melting point compared to graphene, especially in vacuum environments. In graphene the main mechanisms of electron energy relaxation are: scattering with acoustic phonons, impurities and phonons (supercollisions), and optical phonons for very low, intermediate, and extremely high temperatures, respectively [6,7]. Energy relaxation is found to increase with disorder produced by thermal treatment [8] or by optically added defects [9].

It is understood that inelastic scattering by optical phonons or surface polar phonons is responsible for current saturation at high fields [2,10–15]. In a typical device with disorder, however, the current never saturates completely because it is sensitive to elastic scattering processes [2,13] and Joule self-heating of the device [14,15]. A study of this transport regime, which gives valuable information about elastic scattering processes, requires knowledge of the temperature, ideally during the whole voltage ramp. Usually this is achieved by estimation through the heat diffusive equation [15,16] or by independent Raman spectroscopy [11] or Scanning

\* Corresponding author.

\*\* Corresponding author.

E-mail addresses: [charalambos.evangelis@materials.ox.ac.uk](mailto:charalambos.evangelis@materials.ox.ac.uk) (C. Evangelis), [okolosov@lancaster.ac.uk](mailto:okolosov@lancaster.ac.uk) (O.V. Kolosov).

<sup>1</sup> Equal Contribution.

Thermal Microscopy [17,18] measurements.

In this work, we study momentum-relaxation mechanisms of electrons during transport in bowtie-shaped nanoscale graphene devices at room temperature and high-vacuum. We increase the degree of disorder in a controlled manner, by feedback-controlled voltage ramps at high-current densities close to the breakdown limit while monitoring the temperature with a scanning thermal microscope (SThM). We develop a phenomenological model that takes into account self-heating at low and intermediate bias, and we show that the electron-phonon momentum scattering rate increases with increased disorder at room temperature. After considering different possible origins of this observation, such as changes in the charge density or activation of optical phonons, we conclude that new acoustic phonon channels are enabled, possibly due to strong disorder-assisted phonon scattering.

## 2. Experimental

**Device fabrication.** The graphene is grown via chemical vapor deposition (Graphenea S.A.) and transferred onto a pre-patterned doped Si wafer substrate with 300nm of SiO<sub>2</sub> and Cr/Au electrodes. The graphene is patterned into a 200nm wide bowtie-shaped constriction using electron-beam lithography and oxygen plasma etching [19]. This process results in fabrication of many identical devices. Graphene quality is checked with Raman spectroscopy, atomic force microscopy (AFM) and scanning electron microscopy (SEM) measurements (see SI note 4 for characteristic examples).

**Scanning Thermal Microscopy.** To simultaneously study the electrical and thermal properties of a graphene bowtie nano-constriction, we have developed a specialized high-vacuum chamber equipped with a SThM for thermal imaging [20,21] and feed-throughs for electrical characterization. SThM operates like a conventional AFM, except that a resistive implant on the cantilever close to the tip acts as a heater and thermometer at the same time that is sensitive to the local temperature and thermal resistance variations of the tip-sample contact. The probe forms one leg of a balanced Wheatstone bridge operating at 91 kHz, with the bridge output amplified via a low-noise instrumental amplifier, producing the raw SThM signal. We apply an AC and DC voltage to the probe and it is heated to a temperature a few K higher than the microscope temperature, which is monitored with a surface mount Pt resistor. When the tip is in contact with the sample, the resistance of the probe changes depending on the temperature and thermal resistance of the sample [22]. Out of the SThM signal we can map [23] or monitor the local variation (see SI note 1) of temperature. The SThM signal is converted to temperature through probe electrical resistance versus temperature calibration [24] performed in the high-vacuum chamber and modeling of the tip-sample thermal circuit (see SI note 1).

**Temperature measurement at high current densities.** We first apply a small bias voltage across the devices ( $V_b = 0.5V$ ) to spatially map the temperature [23]. Next, to investigate the electrical and thermal properties of the graphene nano-constriction when a large bias voltage, close to the breakdown limit, is applied across it, we place the SThM tip where the highest temperature was detected. We simultaneously monitor the current and temperature whilst we increase the voltage across the nano-constriction. To prevent uncontrolled electrical breakdown of the graphene, we employ a feedback method [25]. This method allows us to controllably Joule heat the graphene to the maximum limit, where the breakdown initiates and gradually increase the amount of disorder in the nano-constriction via a cyclical process. During each cycle the voltage across the constriction is slowly ( $5 - 8Vs^{-1}$ ) ramped up from zero. When the current through the constriction begins to drop, due to

the onset of breakdown of the graphene, the voltage is quickly ( $2500 - 5000Vs^{-1}$ ) ramped down to zero.

## 3. Results and discussion

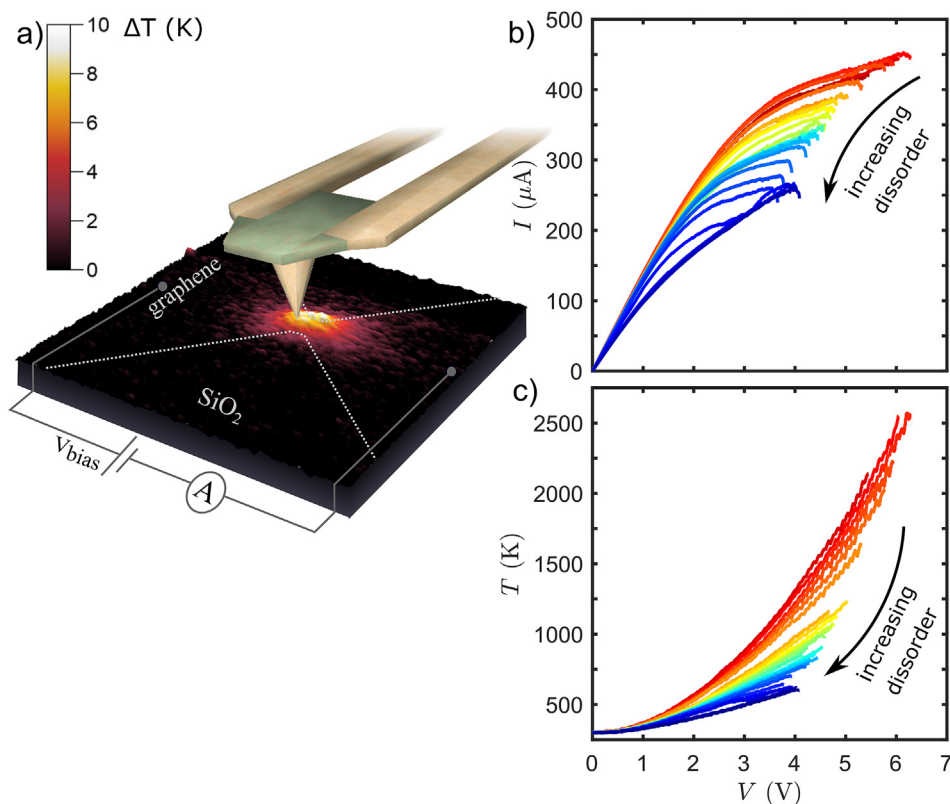
### 3.1. Feedback-controlled breakdown

Fig. 1a shows a typical temperature map: the temperature is highest near the narrow part of the graphene constriction due to the higher current density and resulting Joule heating in this region [18]. The temperature increase is localized to the graphene and SiO<sub>2</sub> area near the constriction as a result of the poor thermal conductivity of SiO<sub>2</sub> and the SiO<sub>2</sub>/graphene interface, which makes the nano-constriction an inefficient heat spreader despite the high thermal conductivity of the graphene [20].

By comparing the current and temperature traces as a function of bias voltage (see Fig. 1b and c), we observe that: i) the differential conductance  $dI/dV_b$  decreases with increasing temperature in each cycle; and ii) the maximum current and temperature that are reached before the onset of breakdown decrease from one cycle to the next. Examples of the same measurements on two additional devices with similar qualitative characteristics are presented in the SI note 3. We note here that even if the qualitative trend of the temperature with the number of cycles is robust for each device, comparison between the temperature maps or traces for different devices is non-trivial due to the SThM tip and contact thermal resistance influence on the measurement (see SI note 1). In the next sections we will show how these observations reveal an increase in the electron-phonon scattering rate with increasing disorder in the graphene nano-constriction.

When we investigate the current-voltage ( $I - V$ ) curves for individual cycles, we observe that these can be either concave downward ( $d^2I/dV^2 < 0$ ) or concave upward ( $d^2I/dV^2 > 0$ ) (see Fig. 2a–c and SI note 3 for more examples). This separation is further evidenced by a statistical analysis of the zero-bias conductance of a total of 10,634 cycles measured over 138 devices, as shown in Fig. 2. We find that the large majority of concave downward curves have a zero-bias conductance greater than the conductance quantum  $G_0 = 2e^2/h = 7.7 \times 10^{-5}S$ , which we therefore attribute to diffusive transport. The concave-upward curves have a zero-bias conductance less than  $G_0$  and we therefore attribute these to transport across single or multiple potential barriers. The transition from diffusive transport to transport across one or more potential barriers is a direct result of the gradually increasing disorder in the graphene nano-constriction. At the end of each cycle, Joule heating leads to an increase in the number of scattering sites which eventually form potential barriers in the graphene nano-constriction. While the atomistic details of this process are not known, studies of electric breakdown of graphene under different atmospheres have suggested that - depending on the oxygen concentration of the sample surroundings - Joule heating either leads to oxidation or sublimation of the graphene [19,26,27], thereby increasing the amount of disorder.

The concave-upward curves at room temperature for  $G < G_0$  are consistent with our previous observation of the gradual transition from multi-mode Fabry-Pérot interference to sequential electron tunneling (Coulomb blockade) across one or more graphene islands to the formation of tunnel junctions with decreasing conductance below  $G_0$  at cryogenic temperatures [28]. The appearance of peaks in the conductance histogram could point to the preferential formation of specific atomic configurations, such as carbon chains [29–31], or be related to transport through the SiO<sub>2</sub>/graphene interface [32]. Unravelling the details of tunneling transport of graphene constrictions with unknown characteristics is complex and beyond the scope of this study.



**Fig. 1.** (a) Schematic representation of the in-situ measurement, with a typical temperature map of the graphene nano-constriction (scan dimensions  $2.5 \times 2.5 \mu m$ ). Color bar indicates the excess temperature with respect to room temperature ( $\Delta T = T - T_0$ ) (b,c) Current vs voltage curves of the initial cycles of feedback-controlled breakdown of graphene devices (b) and the corresponding temperature during the process (c). (A colour version of this figure can be viewed online.)

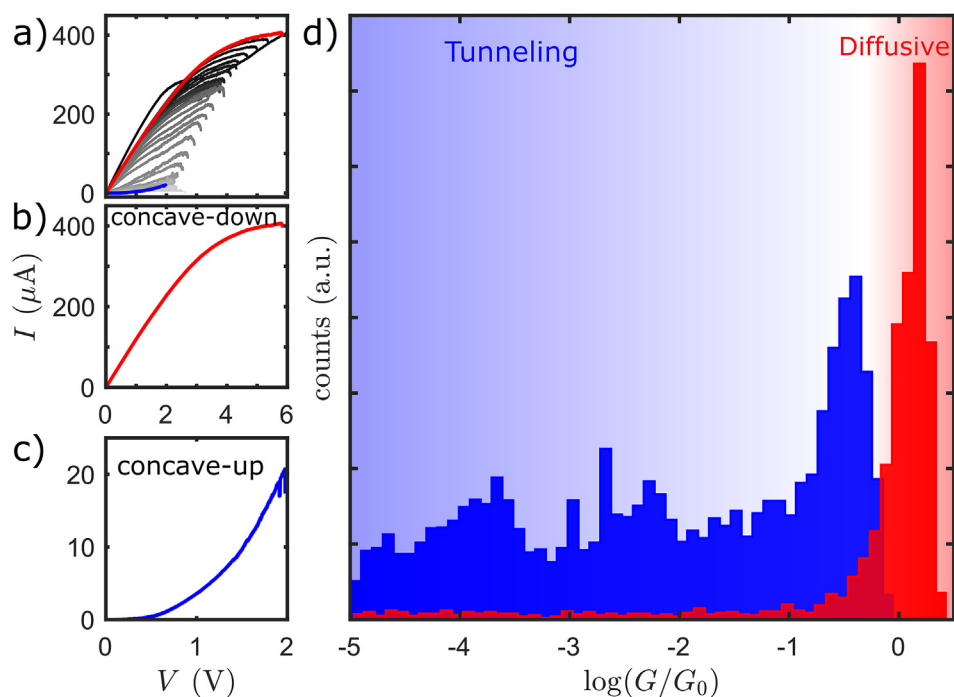


**Fig. 2.** (a) Typical example of  $I-V$  curves during the feedback-controlled breakdown process. (b,c) Examples of  $I-V$  curves showing: high-field diffusive (b) and tunneling (c) transport. (d) Histogram of zero-bias conductance ( $\log(G/G_0)$ ) for cycles with tunneling behaviour (blue) and high-field diffusive transport (red) for 138 devices. (A colour version of this figure can be viewed online.)

In the following we focus on electronic and thermal transport in the diffusive transport regime. In this regime, we never observe superlinear  $I-V$  characteristics, which could indicate Zener-tunneling processes [33]. Initially, we quantify the effect of voltage cycles on the disorder of a typical device, by performing gate dependent current measurements (See SI information note 2) after each cycle. We found that the mobility has a tendency to decrease with the number of cycles and is in the range of  $100 - 200 \text{ cm}^2 \text{ V}^{-1} \text{ sec}^{-1}$ , at carrier densities higher than  $5 \times 10^{-12} \text{ cm}^{-2}$ .

### 3.2. Phenomenological model of Joule heating and electronic transport

In the diffusive transport regime the current initially increases linearly with voltage and gradually tends to saturate (see Fig. 1b). The maximum current density in the constriction, calculated for the first  $I-V$  cycle, is  $9.1 \times 10^8 \text{ A cm}^{-2}$  which is of the same order as previously reported for graphene devices [34]. Current saturation at high field is attributed to optical phonon activation, and we can use an interpolation formula [13–15] to fit the  $I-V$  curves and extract the saturation current  $I_{\text{sat}}$

$$I = \frac{G_0 V}{\left[ 1 + \left( \frac{G_0 V}{I_{\text{sat}}} \right)^{n-1} \right]^{1/n}}, \quad (1)$$

where  $G_0$  is the zero-bias conductance which is measured after each cycle. In principle, parameter  $n$  could be considered to be a fitting parameter, but we choose  $n = 2$  [15] corresponding to  $I-V$  characteristics containing only odd terms in  $V$  which is consistent with spatial inversion symmetry. In Fig. 3 examples of fitted  $I-V$  curves for different cycles are shown (note that  $I-V$ s are shifted in the x-axis for clarity). The maximum current of the experimental curves does not reach the fit value of  $I_{\text{sat}}$ , which we attribute to elastic scattering processes [2,13] and Joule heating of the device [14,15]. We further observe that the fit value of  $I_{\text{sat}}$  decreases with the number of cycles (see Fig. 3b).

Since our  $I-V$  curves generally do not reach the regime of current saturation (where emission of optical phonons would dominate), we focus on the role of Joule self-heating at low and intermediate bias. To this end, we develop a phenomenological model that takes into account self-heating in the  $I-V$  characteristics up to cubic order in  $V$ . This model assumes that the low bias conductance has a Drude form  $G \propto \tau(T)$ , and that the momentum relaxation time  $\tau(T)$  decreases as the temperature  $T$  increases due to Joule self-heating with power  $P = IV$ . In particular, we expand  $G(T)$  around room temperature,  $T_0$ , as

$$G(T) = G(T_0) \left( 1 + \Delta T \frac{1}{\tau} \frac{d\tau}{dT} \Big|_{T=T_0} + \dots \right), \quad (2)$$

where  $G(T_0) = c\tau(T_0)$  and the temperature rise  $\Delta T = T - T_0$  due to Joule heating is related to the power  $P$  injected. By expanding  $T(P)$  at  $T_0$ , with  $T_0 = T(0)$ , the temperature rise in the device may be written as

$$\Delta T = P \frac{dT}{dP} \Big|_{T=T_0} + \dots, \quad (3)$$

and by substituting Equations (2) and (3) in  $I = GV$  with  $P = IV$ , we obtain the following expression for the current, valid up to cubic order in  $V$ ,

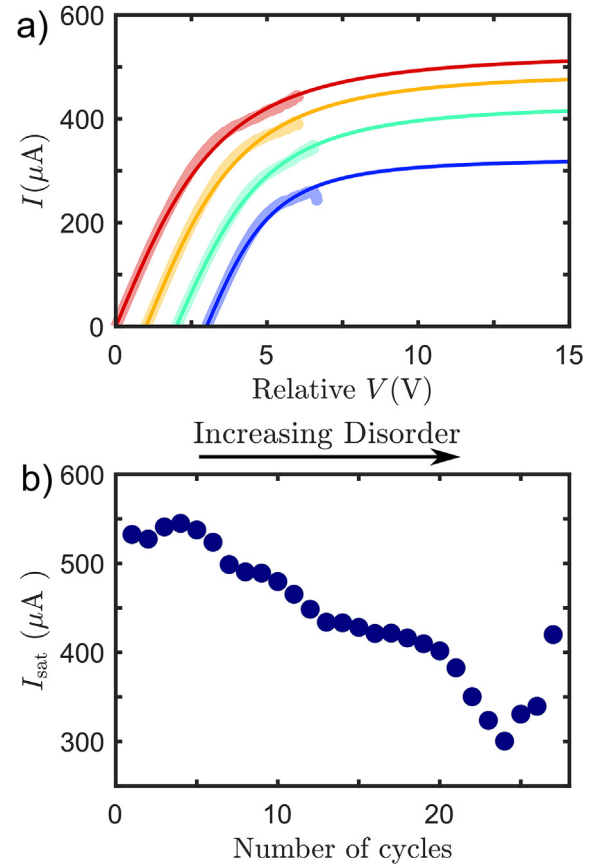


**Fig. 3.** (a) Examples of measured (thick transparent line) and fitted from Equation (1) (solid line)  $I-V$  curves. Note that the examples are curves taken from the device presented in Fig. 1 of the 2nd (red), 8th (orange), 15th (green) and 23rd (blue) cycle and are shifted in the x-axis for clarity. (b) Saturation current as a function of cycles as obtained by fitting Equation (1) to the  $I-V$  curves of Fig. 1b. (A colour version of this figure can be viewed online.)

$$I = G(T_0)V - \gamma G^2(T_0)V^3 + \dots, \quad (4)$$

where  $\gamma = - \frac{dT}{dP} \frac{1}{\tau} \frac{d\tau}{dT} \Big|_{T=T_0} = \frac{dT}{dP} \frac{d \ln \tau^{-1}}{dT} \Big|_{T=T_0}$ . Note that, since we consider the logarithmic derivative, the argument of the logarithm does not need to be dimensionless. Hence, the logarithmic derivative of the momentum scattering rate with respect to temperature, i.e. the relative change of the momentum scattering rate (RCSR) at room temperature, is given by

$$\frac{d}{dT} \ln \tau^{-1} \Big|_{T=T_0} = \frac{\gamma}{dT/dP \Big|_{T=T_0}}. \quad (5)$$

It is possible to determine the RCSR from the experimental data because  $dT/dP|_{T=T_0}$  and  $\gamma$  are fitting parameters of Equations (3) and (4) to the temperature vs power  $P-T$  and  $I-V$  characteristics of each cycle, respectively. Fig. 4 a and b shows representative examples of fitted  $I-V$  and  $P-T$  curves. For the  $I-V$ , the cubic term is small as compared to the first one for  $V < (\gamma G(T_0))^{-1/2}$ , and we have checked that  $V$  is in this regime for the whole of the fitting.

From Equation (2) it can be seen that the RCSR at  $T_0$  is the negative derivative of the normalized (by zero-bias conductance) conductance with respect to temperature,  $d(G/G(T_0))/dT$ . Fig. 4c shows examples of  $G/G(T_0)$ , with temperature for different cycles and therefore degrees of disorder.  $G$  is defined as  $G = I/V$  evaluated

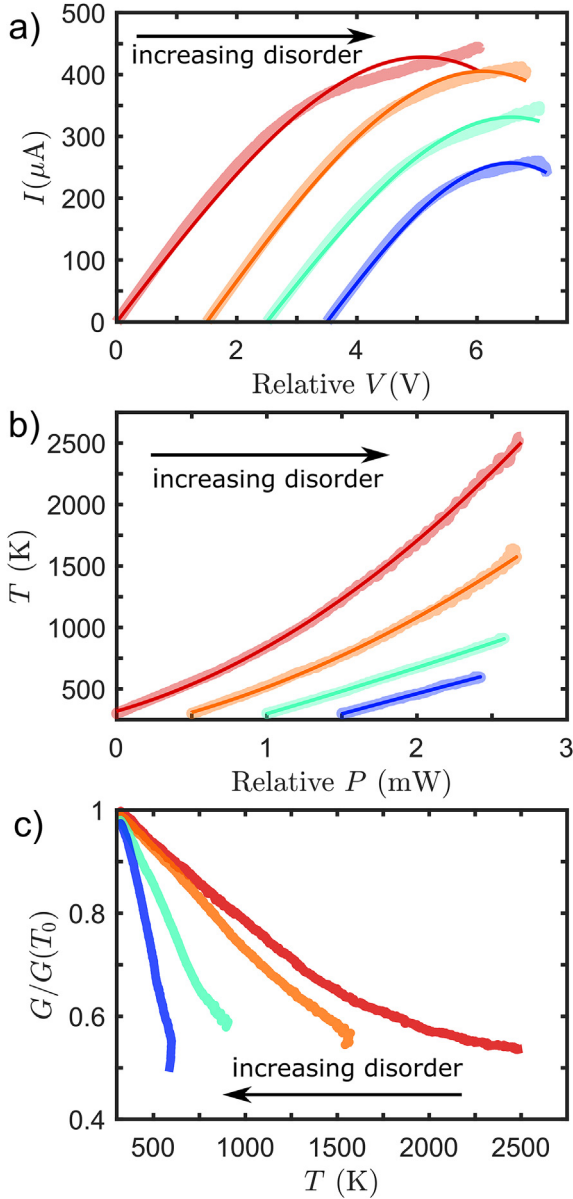


**Fig. 4.** (a,b) Examples of measured (thick transparent line) and fitted from the model (solid line)  $I-V$  (a) and  $T-P$  (Power is calculated arithmetically from each  $I-V$  curve) curves (b). For the fits we used Equations (3) and (4) for  $T-P$  and  $I-V$  curves, respectively, with up to 3rd order terms included. Note that the examples are curves taken from the device presented in Fig. 1 of the 2nd (red), 6th (orange), 15th (green) and 23rd (blue) cycle and are shifted in the x-axis for clarity. (c) Normalized by  $G(T_0)$  conductance,  $G$ , with temperature evaluated at each data point on the  $I-V$  traces in (a). (A colour version of this figure can be viewed online.)

at each data point on the  $I-V$  curve and  $G(T_0)$  the zero-bias conductance measured after each cycle. Unexpectedly, we find that the negative derivative of  $G/G(T_0)$  at  $T_0$ , and thus the RCSR at  $T_0$ , increases with disorder. One would expect the opposite, since  $\tau^{-1}$  itself increases with increasing disorder.

To systematically extract the RCSR as a function of disorder we express  $I$  as

$$I = \frac{1}{2\gamma V} \left( \sqrt{1 + 4\gamma G(T_0)V^2} - 1 \right), \quad (6)$$

which agrees with Equation (4) up to cubic order in  $V$ . Equation (6) (see SI note 5 for derivation) provides a better fit (see SI note 2 for

examples) than truncating the expression at cubic order in  $V$ ; Equation (6) predicts  $I \rightarrow \text{const}$  as  $V \rightarrow \infty$  whereas truncating at cubic order as in Equation (4) gives a wholly unphysical result  $I \rightarrow -\infty$  as  $V \rightarrow \infty$ . We use Equation (6) to fit the  $I-V$  characteristics of each cycle and obtain  $G(T_0)$  and  $\gamma$  (see Fig. 5 a and b, respectively).  $G(T_0)$  generally decreases with the number of cycles with individual values being very close to the zero-bias conductance as measured after each cycle (see SI note 2).  $\gamma$ , on the other hand, increases up to a point and then starts to decrease at a high degree of disorder. To calculate the RCSR with disorder we further fit  $P-T$  curves with Equation (3) and obtain  $|dT/dP|_{T=T_0}$  (see Fig. 5c). The RCSR is found to increase with disorder, however for a high degree of disorder it drops sharply (see Fig. 5d). This drop is related to the sharp resistance decrease (see Fig. 5a) and possibly indicates a transition to different transport regime (e.g. tunneling), not described by our model. Similar trends are obtained for two additional devices (see SI note 3).

To understand this counter-intuitive result, we take into account disorder and phonons as sources of momentum relaxation. We assume a temperature-independent scattering rate  $\tau_d^{-1}$  due to static disorder such as charged Coulomb impurities or vacancies and a number of temperature-dependent electron-phonon rates  $\tau_i^{-1}(T)$ , where  $i$  indexes different phonon modes, so that  $\tau^{-1} = \tau_d^{-1} + \sum_i \tau_i^{-1}(T)$  and

$$\frac{d}{dT} \ln \tau^{-1} \Big|_{T=T_0} = \frac{\sum_i \Delta_i(T_0)}{\tau_d^{-1} + \sum_i \tau_i^{-1}(T_0)}, \quad (7)$$

where  $\Delta_i(T_0) = \frac{d}{dT} (\tau_i^{-1}(T)) \Big|_{T=T_0}$ . In other words, the RCSR at  $T_0$  is given by the change of the scattering rates due to phonons divided by the total scattering rate, all evaluated at temperature  $T_0$ .

Assuming that scattering rates due to acoustic phonons exhibit a generic power-law dependence on temperature  $\tau_\alpha^{-1}(T) \sim T^\alpha$ , then  $\Delta_\alpha(T_0) \sim \alpha T_0^{\alpha-1}$  (theory predicts that  $\alpha = 1$  for graphene near room temperature) [35,36]. At room temperature and near the chemical potential (as is appropriate for the low and intermediate bias regime), the rate due to optical phonons with frequency  $\omega_0$  will be exponentially suppressed  $\tau_\omega^{-1}(T) \sim \exp(-\hbar\omega/k_B T_0)$  yielding  $\Delta_\omega(T_0) \sim \hbar\omega/k_B T_0^2 \exp(-\hbar\omega/k_B T_0)$  (see SI note 7). Given that  $\omega_0 \approx 200 \text{meV}$  in graphene [12,37,38], this contribution is very small at room temperature  $T_0$ , and we neglect it in the following.

Before focusing on disorder, we briefly discuss the dependence of  $\tau^{-1}$  on charge density, which may also change with cycle number. The disorder rate  $\tau_d^{-1}$  originating from charge impurities or vacancies is predicted to decrease with charge density [36] while the acoustic phonon rate should increase with density [35,36]. Thus, an increase of charge density with cycle number would explain the observed behavior of  $\tau^{-1}$ . To check this hypothesis, we swept the back-gate voltage of our devices while recording the current after each voltage ramp cycle (see SI note 2). We found that the Dirac point minimum becomes less defined after each cycle which is consistent with an increase in disorder, but it shifts from positive gate voltages towards zero with increasing number of cycles. This would indicate a decrease of charge density which is the opposite trend to what is needed to explain the observed behavior of the scattering rate.

The scattering rate due to disorder  $\tau_d^{-1} = v_F/l$ , where  $v_F$  is the Fermi velocity and  $l$  is the electron mean free path, increases with the degree of disorder. For the RCSR to increase with disorder, as is observed, the scattering rate due to phonons ( $\tau_p^{-1}$ ) must increase with disorder faster than  $\tau^{-1}$  itself (where  $\tau^{-1} \geq \tau_d^{-1}$ ). We attribute

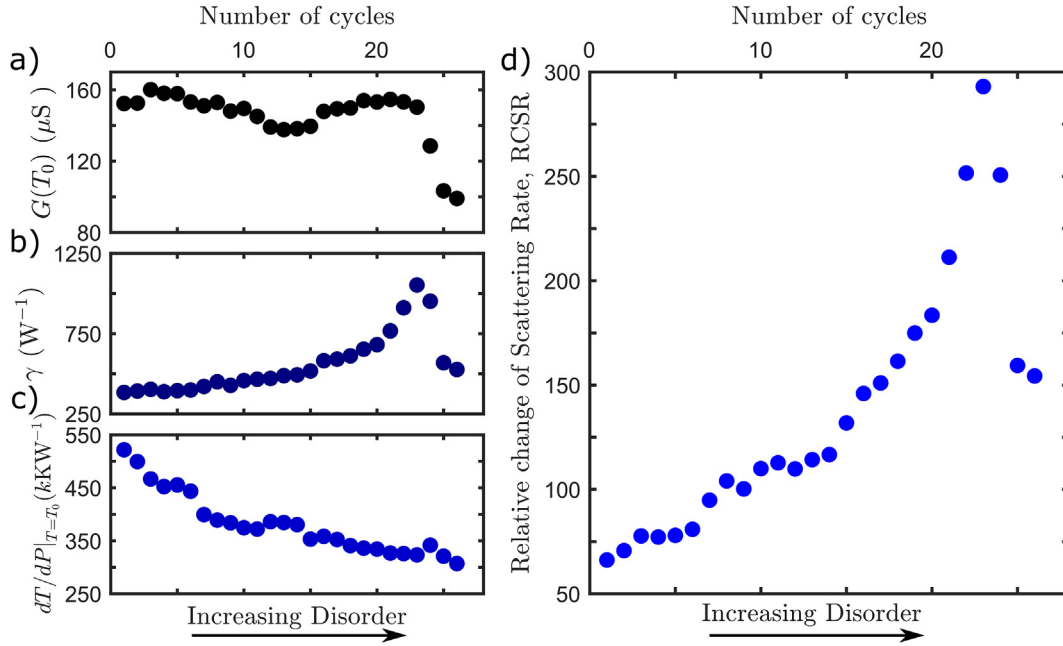


**Fig. 5.** (a,b,c,d) Conductance at room temperature  $G(T_0)$  (a), parameter  $\gamma$  (b),  $|dT/dP|_{T=T_0}$  (c) and relative change of momentum scattering rate (RCSR) (d) with the number of cycles (i.e. increasing disorder) for the device presented in Fig. 1.  $G(T_0)$ ,  $\gamma$  and  $|dT/dP|_{T=T_0}$  are extracted by fitting Equations (6) and (3) to the  $I-V$  and  $P-T$  curves presented in Fig. 1 and then are used for the calculation RCSR with Equation (5). (A colour version of this figure can be viewed online.)

this behavior to new phonon scattering channels that open up as disorder increases. Theoretical modeling of electron momentum relaxation due to acoustic phonons in graphene has focused on the ballistic limit [35,36] whereby

$$\tau_{\text{ballistic}}^{-1}(T) = \frac{2\pi}{\hbar} \lambda k_B T, \quad (8)$$

where  $\lambda$  is the dimensionless electron-phonon coupling constant. Disorder-assisted phonon scattering events, known as supercollisions, have been discussed at length in the context of electron cooling [7,8,39]. Using a perturbative calculation for weak disorder  $k_F l \gg 1$ , where  $k_F$  is the Fermi wavevector, Song et al. [39] considered the influence of supercollisions on momentum relaxation,

$$\tau_{\text{super}}^{-1}(T) = \frac{4\pi}{\hbar k_F l} \lambda k_B T \ln(T/T_{\text{BG}}), \quad (9)$$

where  $T_{\text{BG}}$  is the Bloch-Grüneisen temperature and  $T_0 \gg T_{\text{BG}}$ . The supercollision rate  $\tau_{\text{super}}^{-1}(T)$  increases with the degree of disorder (as  $k_F l$  decreases). If it were the only acoustic rate,  $\tau_{\text{ballistic}}^{-1}(T)$  would ensure the RCSR decreases with disorder, the opposite trend to that observed, whereas the addition of  $\tau_{\text{super}}^{-1}(T)$  would lead to a saturation of the RCSR. We stress that the supercollision rate  $\tau_{\text{super}}^{-1}(T)$  is only first order in the perturbative parameter  $1/k_F l$  and we speculate that there are yet more channels for electron-phonon scattering that become relevant as the degree of disorder increases and that dominate in the limit of strong disorder  $k_F l \sim 1$ . Indeed, in the context of thermal transport, numerical modelling has shown that vacancies induce localization of acoustic phonons which leads to a drastic reduction in thermal conductivity [40,41]. An indication of what could happen with electron-phonon scattering is given by examining the form of the electron-phonon coupling constant in the deformation potential approximation,  $\lambda \sim v_\alpha^{-2}$  where  $v_\alpha$  is the phonon velocity. This suggests phonon localization due to vacancies should dramatically enhance  $\lambda$  and the electron-phonon

scattering rate; such an increase could account for the increase with disorder of the RCSR observed in our experiments.

Although our study of momentum relaxation only required us to consider Joule heating in a general way, as in Equation (3), it is possible to extract further information about heat transport from our data. As described in detail in the SI (see SI note 6), we assume that the thermal conductivity is independent of temperature and that the heat is dissipated into the substrate, rather than, say, via electron thermalization in the leads. Then, under the condition that the thermal healing length ( $L_H = \sqrt{\kappa R_B}$ ) [42] is much shorter than the system size, the slope of the  $T(P)$  curve,  $|dT/dP|_{T=T_0}$ , is equivalent to the thermal resistance  $R_B$  of the graphene/SiO<sub>2</sub> interface per unit area  $R_B/A$  ( $A$  is the surface area of graphene). Hence, Fig. 5c shows that  $R_B/A$  decreases with the number of cycles meaning that more power can be dissipated into the substrate for a certain temperature as the disorder increases. This might be a result of some changes in the effective graphene size and/or the interface with SiO<sub>2</sub>. More specifically, a decrease of the effective size of the device is possible due to sublimation of graphene; naively, a reduction of  $A$  should increase the ratio  $R_B/A$  but, at the same time, reduced size can actually improve dissipation via 3D heat spreading into the substrate [4]. The high local temperatures might also account for some changes in the graphene/SiO<sub>2</sub> interface (eg. sublimation of trapped adsorbates) resulting in better heat dissipation to the substrate.

#### 4. Outline

In summary, we studied the momentum-relaxation mechanisms of electrons with increased disorder by measuring the temperature of a graphene device while ramping the bias voltage to the breakdown limit. By feedback-controlled voltage ramps the graphene is Joule heated and the amount of disorder is controllably increased. We developed a model for calculating the relative change of the momentum scattering rate with temperature from the current-voltage and temperature-power characteristics

acquired during the process. By applying the model we show that the relative change of the momentum scattering rate increases with disorder at room temperature as a result of the increased electron-phonon scattering rate. We attribute this to new acoustic phonon scattering channels that open up as disorder increases, possibly due to disorder-assisted phonon scattering. However, for highly disordered graphene, the scattering rate due to disorder increases at a higher rate, possibly indicating a transition to a different transport regime. Finally, we find that the interface thermal resistance decreases with disorder and we associate that with a decrease of the effective size of the graphene due to sublimation and changes in the graphene/SiO<sub>2</sub> interface due to the high temperature. Our correlated conductance and temperature measurements highlight the importance of electronic momentum relaxation due to phonon scattering that limits carrier mobility in disordered graphene nanostructures. In addition to revealing elusive electron-phonon physics in electronic transport, our work has direct implications for the performance of graphene interconnects for next generation CMOS devices.

### Author contributions

C.E. and E.M. contributed equally to this work. J.L.S., X.B. and J.O.T. fabricated the devices. C.E., E.M. and J.A.M. drafted the manuscript. C.E., J.L.S. and O.V.K. performed the SThM measurements and interpretation of SThM data. C.E. and J.O.T. performed the transport measurements. C.E. analyzed and processed the data with the help of S.T. E.M. carried out the theoretical modeling. C.E., O.V.K. and J.A.M. designed the experiments. All authors contributed to manuscript revision and discussion of the results.

### CRediT authorship contribution statement

**Charalambos Evangelì:** Writing - original draft, Conceptualization, Methodology, Validation, Formal analysis, Investigation. **Edward McCann:** Writing - original draft, Conceptualization, Methodology, Validation. **Jacob L. Swett:** Investigation, Writing - review & editing. **Sumit Tewari:** Formal analysis, Writing - review & editing. **Xinya Bian:** Investigation. **James O. Thomas:** Investigation, Writing - review & editing. **G. Andrew D. Briggs:** Funding acquisition, Writing - review & editing, Resources. **Oleg V. Kolosov:** Funding acquisition, Writing - review & editing, Investigation, Methodology, Resources, Conceptualization. **Jan A. Mol:** Funding acquisition, Writing - review & editing, Methodology, Resources, Conceptualization.

### Declaration of competing interest

The authors declare that they have no known competing financial interests or personal relationships that could have appeared to influence the work reported in this paper.

### Acknowledgements

C.E., J.L.S., S.T., X.B., J.O.T., J.A.M. and G.A.D.B. acknowledge the QuEEN Programme Grant (EP/N017188/1). C.E. and G.A.D.B. acknowledge the John Templeton Foundation. O.V.K. acknowledges the GrapheneCore3 grant number 881603 (Graphene Flagship), EU project QUANTIHEAT (Grant 604668), EPSRC project EP/K023373/1, UKRI project NEXGENNA and Paul Instrument Fund, c/o The Royal Society. J.A.M. was supported through the UKRI Future Leaders Fellowship, Grant No. MR/S032541/1, with in-kind support from the Royal Academy of Engineering.

### Appendix A. Supplementary data

Supplementary data to this article can be found online at <https://doi.org/10.1016/j.carbon.2020.12.012>.

### References

- [1] J. Jiang, J.H. Chu, K. Banerjee, Cmos-compatible doped-multilayer-graphene interconnects for next-generation vlsi, in: 2018 IEEE International Electron Devices Meeting (IEDM), IEEE, 2018, pp. 34–35.
- [2] A. Barreiro, M. Lazzeri, J. Moser, F. Mauri, A. Bachtold, Transport properties of graphene in the high-current limit, *Phys. Rev. Lett.* 103 (7) (2009), 076601.
- [3] S. Berciaud, M.Y. Han, K.F. Mak, L.E. Brus, P. Kim, T.F. Heinz, Electron and optical phonon temperatures in electrically biased graphene, *Phys. Rev. Lett.* 104 (22) (2010) 227401.
- [4] A.D. Liao, J.Z. Wu, X. Wang, K. Tahy, D. Jena, H. Dai, E. Pop, Thermally limited current carrying ability of graphene nanoribbons, *Phys. Rev. Lett.* 106 (25) (2011) 256801.
- [5] S. Islam, Z. Li, V.E. Dorgan, M.-H. Bae, E. Pop, Role of joule heating on current saturation and transient behavior of graphene transistors, *IEEE Electron. Device Lett.* 34 (2) (2013) 166–168.
- [6] Q. Ma, N.M. Gabor, T.I. Andersen, N.L. Nair, K. Watanabe, T. Taniguchi, P. Jarillo-Herrero, Competing channels for hot-electron cooling in graphene, *Phys. Rev. Lett.* 112 (24) (2014) 247401.
- [7] M.W. Graham, S.-F. Shi, D.C. Ralph, J. Park, P.L. McEuen, Photocurrent measurements of supercollision cooling in graphene, *Nat. Phys.* 9 (2) (2013) 103.
- [8] A. Betz, S.H. Jhang, E. Pallicchi, R. Ferreira, G. Fève, J.-M. Berroir, B. Plaças, Supercollision cooling in undoped graphene, *Nat. Phys.* 9 (2) (2013) 109.
- [9] T.V. Alencar, M.G. Silva, L.M. Malard, A.M. de Paula, Defect-induced supercollision cooling of photoexcited carriers in graphene, *Nano Lett.* 14 (10) (2014) 5621–5624.
- [10] I. Meric, M.Y. Han, A.F. Young, B. Ozyilmaz, P. Kim, K.L. Shepard, Current saturation in zero-bandgap, top-gated graphene field-effect transistors, *Nat. Nanotechnol.* 3 (11) (2008) 654.
- [11] M. Freitag, M. Steiner, Y. Martin, V. Perebeinos, Z. Chen, J.C. Tsang, P. Avouris, Energy dissipation in graphene field-effect transistors, *Nano Lett.* 9 (5) (2009) 1883–1888.
- [12] R. Shishir, D. Ferry, Velocity saturation in intrinsic graphene, *J. Phys. Condens. Matter* 21 (34) (2009) 344201.
- [13] J. Chauhan, J. Guo, High-field transport and velocity saturation in graphene, *Appl. Phys. Lett.* 95 (2) (2009), 023120.
- [14] V. Perebeinos, P. Avouris, Inelastic scattering and current saturation in graphene, *Phys. Rev. B* 81 (19) (2010) 195442.
- [15] V.E. Dorgan, M.-H. Bae, E. Pop, Mobility and saturation velocity in graphene on sio 2, *Appl. Phys. Lett.* 97 (8) (2010), 082112.
- [16] V.E. Dorgan, A. Behnam, H.J. Conley, K.I. Bolotin, E. Pop, High-field electrical and thermal transport in suspended graphene, *Nano Lett.* 13 (10) (2013) 4581–4586.
- [17] Y.-J. Yu, M.Y. Han, S. Berciaud, A.B. Georgescu, T.F. Heinz, L.E. Brus, K.S. Kim, P. Kim, High-resolution spatial mapping of the temperature distribution of a joule self-heated graphene nanoribbon, *Appl. Phys. Lett.* 99 (18) (2011) 183105.
- [18] A. Harzheim, J. Spiece, C. Evangelì, E. McCann, V. Falko, Y. Sheng, J.H. Warner, G.A.D. Briggs, J.A. Mol, P. Gehring, O.V. Kolosov, Geometrically enhanced thermoelectric effects in graphene nanoconstrictions, *Nano Lett.* 18 (12) (2018) 7719–7725.
- [19] C.S. Lau, J.A. Mol, J.H. Warner, G.A.D. Briggs, Nanoscale control of graphene electrodes, *Phys. Chem. Chem. Phys.* 16 (2014) 20398–20401.
- [20] C. Evangelì, J. Spiece, S. Sangtarash, A.J. Molina-Mendoza, M. Mucientes, T. Mueller, C. Lambert, H. Sadeghi, O. Kolosov, Nanoscale thermal transport in 2d nanostructures from cryogenic to room temperature, *Adv. Electron. Mater.* 5 (10) (2019) 1900331.
- [21] M.E. Pumarol, M.C. Rosamond, P. Tovee, M.C. Petty, D.A. Zeze, V. Falko, O.V. Kolosov, Direct nanoscale imaging of ballistic and diffusive thermal transport in graphene nanostructures, *Nano Lett.* 12 (6) (2012) 2906–2911.
- [22] J. Spiece, C. Evangelì, K. Lulla, A. Robson, B. Robinson, O. Kolosov, Improving accuracy of nanothermal measurements via spatially distributed scanning thermal microscope probes, *J. Appl. Phys.* 124 (1) (2018), 015101.
- [23] F. Menges, H. Riel, A. Stemmer, B. Gotsmann, Quantitative thermometry of nanoscale hot spots, *Nano Lett.* 12 (2) (2012) 596–601.
- [24] P. Tovee, M. Pumarol, D. Zeze, K. Kjoller, O. Kolosov, Nanoscale spatial resolution probes for scanning thermal microscopy of solid state materials, *J. Appl. Phys.* 112 (11) (2012) 114317.
- [25] P. Gehring, A. Harzheim, J. Spiece, Y. Sheng, G. Rogers, C. Evangelì, A. Mishra, B.J. Robinson, K. Porfyrakis, J.H. Warner, et al., Field-effect control of graphene–fullerene thermoelectric nanodevices, *Nano Lett.* 17 (11) (2017) 7055–7061.
- [26] F. Prins, A. Barreiro, J.W. Ruitenbergh, J.S. Seldenthuis, N. Aliaga-Alcalde, L.M.K. Vandersypen, H.S.J. van der Zant, Room-temperature gating of molecular junctions using few-layer graphene nanogap electrodes, *Nano Lett.* 11 (11) (2011) 4607–4611.
- [27] M. El Abbassi, L. Pósa, P. Makk, C. Nef, K. Thodkar, A. Halbritter, M. Calame, From electroburning to sublimation: substrate and environmental effects in

- the electrical breakdown process of monolayer graphene, *Nanoscale* 9 (2017) 17312–17317.
- [28] P. Gehring, H. Sadeghi, S. Sangtarash, C.S. Lau, J. Liu, A. Ardavan, J.H. Warner, C.J. Lambert, G.A.D. Briggs, J.A. Mol, Quantum interference in graphene nanoconstrictions, *Nano Lett.* 16 (7) (2016) 4210–4216, <https://doi.org/10.1021/acs.nanolett.6b01104>.
- [29] H. Sadeghi, J.A. Mol, C.S. Lau, G.A.D. Briggs, J. Warner, C.J. Lambert, Conductance enlargement in picoscale electroburnt graphene nanojunctions, *Proc. Natl. Acad. Sci. Unit. States Am.* 112 (9) (2015) 2658–2663.
- [30] S.G. Sarwat, P. Gehring, G. Rodriguez Hernandez, J.H. Warner, G.A.D. Briggs, J.A. Mol, H. Bhaskaran, Scaling limits of graphene nanoelectrodes, *Nano Lett.* 17 (6) (2017) 3688–3693.
- [31] J.K. Lee, G.-D. Lee, S. Lee, E. Yoon, H.L. Anderson, G.A.D. Briggs, J.H. Warner, Atomic scale imaging of reversible ring cyclization in graphene nanoconstrictions, *ACS Nano* 13 (2) (2019) 2379–2388.
- [32] L. Pósa, M. El Abbassi, P. Makk, B. Santa, C. Nef, M. Csontos, M. Calame, A. Halbritter, Multiple physical time scales and dead time rule in few-nanometers sized graphene–sio x-graphene memristors, *Nano Lett.* 17 (11) (2017) 6783–6789.
- [33] N. Vandecasteele, A. Barreiro, M. Lazzeri, A. Bachtold, F. Mauri, Current-voltage characteristics of graphene devices: interplay between zener-klein tunneling and defects, *Phys. Rev. B* 82 (4) (2010), 045416.
- [34] R. Murali, Y. Yang, K. Brenner, T. Beck, J.D. Meindl, Breakdown current density of graphene nanoribbons, *Appl. Phys. Lett.* 94 (24) (2009) 243114.
- [35] E. Hwang, S. Adam, S. Das Sarma, Carrier transport in two-dimensional graphene layers, *Phys. Rev. Lett.* 98 (18) (2007) 186806.
- [36] T. Stauber, N. Peres, F. Guinea, Electronic transport in graphene: a semi-classical approach including midgap states, *Phys. Rev. B* 76 (20) (2007) 205423.
- [37] T. Sohier, M. Calandra, C.-H. Park, N. Bonini, N. Marzari, F. Mauri, Phonon-limited resistivity of graphene by first-principles calculations: electron-phonon interactions, strain-induced gauge field, and Boltzmann equation, *Phys. Rev. B* 90 (12) (2014) 125414.
- [38] H. Suzuura, T. Ando, Electron lifetime due to optical-phonon scattering in a graphene sheet, in: *Journal of Physics: Conference Series*, vol. 150, IOP Publishing, 2009, 022080.
- [39] J.C. Song, M.Y. Reizer, L.S. Levitov, Disorder-assisted electron-phonon scattering and cooling pathways in graphene, *Phys. Rev. Lett.* 109 (10) (2012) 106602.
- [40] M. Noshin, A.I. Khan, I.A. Navid, H.A. Uddin, S. Subrina, Impact of vacancies on the thermal conductivity of graphene nanoribbons: a molecular dynamics simulation study, *AIP Adv.* 7 (1) (2017), 015112.
- [41] G. Loh, E.H.T. Teo, B.K. Tay, Phonon localization around vacancies in graphene nanoribbons, *Diam. Relat. Mater.* 23 (2012) 88–92.
- [42] A. Liao, R. Alizadegan, Z.-Y. Ong, S. Dutta, F. Xiong, K.J. Hsia, E. Pop, Thermal dissipation and variability in electrical breakdown of carbon nanotube devices, *Phys. Rev. B* 82 (20) (2010) 205406.